Regeneration of Sulfur-Poisoned Pd-based Catalyst for Natural Gas Oxidation

Mari Honkanen[a,*], Jianguang Wang[b], Marja Kärkkäinen[c], Mika Huuhtanen[c], Hua Jiang[d], Kauko Kallinen[e], Riitta L. Keiski[c], Jaakko Akola[b,f], Minnamari Vippola[a]

[(a)]*Materials Science, Tampere University of Technology, Tampere, Finland*
[(b)]*Physics, Tampere University of Technology, Tampere, Finland*
[(c)]*Environmental and Chemical Engineering, University of Oulu, Oulu, Finland*
[(d)]*Department of Applied Physics, Aalto University, Espoo, Finland*
[(e)]*Dinex Ecocat Oy, Vihtavuori, Finland*
[(f)]*Department of Physics, Norwegian University of Science and Technology, Trondheim, Norway*

[(*)]Corresponding author, email: mari.honkanen@tut.fi, telephone: +358408490133

Co-authors' e-mails: Jianguang Wang: jianguang.wang@tut.fi
Marja Kärkkäinen: marja.karkkainen@oulu.fi
Mika Huuhtanen: mika.huuhtanen@oulu.fi
Hua Jiang: hua.jiang@aalto.fi
Kauko Kallinen: kki@dinex.fi
Riitta L. Keiski: riitta.keiski@oulu.fi
Jaakko Akola: jaakko.akola@tut.fi
Minnamari Vippola: minnamari.vippola@tut.fi

Abstract

Sulfur deactivation and regeneration behavior of the Pd/Al_2O_3 catalyst has been investigated via experimental characterization and density functional theory (DFT) simulations. During the sulfur exposure, PdO crystallites grow slightly while bulk $Al_2(SO_4)_3$ forms on the support. DFT calculations indicate that SO_x species interact strongly with the catalyst surface making it chemically inactive in agreement with the experimental results. During the regeneration treatment (CH_4 conditions), PdO particles reduce, $Al_2(SO_4)_3$ is partially removed, and the activity for CH_4 conversion is increased. No full recovery can be observed due to remaining $Al_2(SO_4)_3$, the formation of encapsulating sulfur species, and the partial reduction of PdO particles. To reoxidize Pd, the catalyst is further regenerated (O_2 conditions). The resulting CH_4 conversion is at the same level than with the regenerated catalyst. Thus, a small amount of $Al_2(SO_4)_3$ appears to have a stronger effect on the performance than the state of Pd.

Keywords

Pd-based catalyst, sulfur poisoning, regeneration, transmission electron microscopy, Fourier transform infrared spectrometry, catalytic testing, density functional theory simulations

Graphical abstract

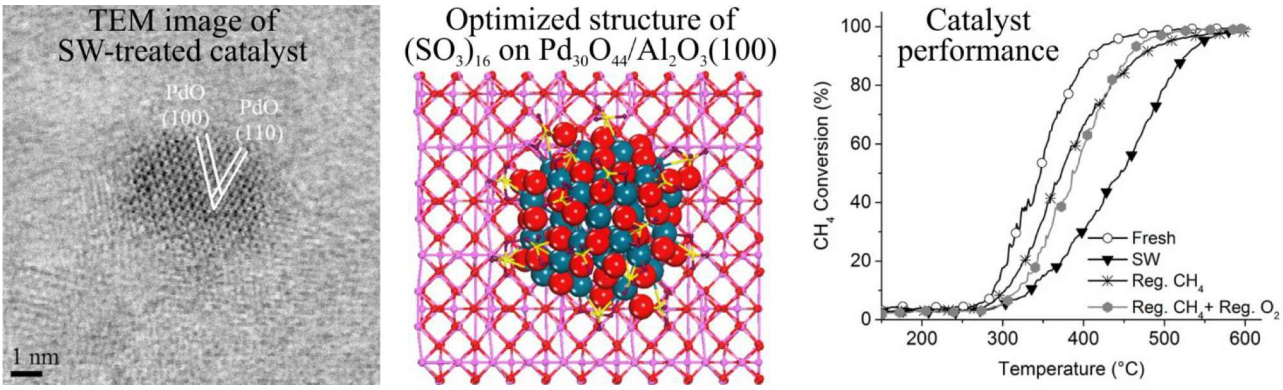

Highlights

- In sulfur treatment, bulk $Al_2(SO_4)_3$ forms and PdO size increases slightly
- Adsorption of $(SO_3)_n$ on $Pd_{30}O_{44}/Al_2O_3$ reaches saturation at n=16
- SO_3 encapsulated $Pd_{30}O_{44}/Al_2O_3$ is chemically inactive
- Regeneration reduces PdO partly to Pd and part of $Al_2(SO_4)_3$ is removed
- Remaining $Al_2(SO_4)_3$ has stronger effect on catalyst performance than state of Pd

1 INTRODUCTION

Transportation is one of the largest sources in air pollution, especially regarding nitrogen oxides (NO_x) and particulate matters (PMs). Thus, emission reduction from vehicle engines is in the top of priority all around the world. The use of natural gas (NG) as an energy source will reduce the NO_x and PM emissions from automotive and heavy-duty vehicles. However, exhaust gases of NG vehicles (NGVs) contain unburned methane which is identified as a strong greenhouse gas and the global warming potential of which is 75 times higher than that of CO_2 [1]. Thus, methane has to be converted to less harmful compounds (CO_2 and H_2O) by a catalytic converter. Pd/Al_2O_3 catalysts are widely known to be very active to combust methane. In addition, it has been concluded that PdO is the active phase while metallic Pd is less active [2,3]. However, the most active phase depends on the operating temperature. Temperature of the exhaust gases from lean-burn NGV engines is typically below 500 – 550 °C [3]. Matam *et al.* [4] have observed that below 677 °C PdO is the active phase for methane combustion, and therefore, PdO is the desirable active phase in the NGV applications.

Problems related to thermal aging and poisoning occur over supported Pd catalysts. Thermal deactivation is caused by the loss of active surface area due to the crystallite growth of noble metal particles, or the collapse of the support, and/or chemical transformations of the active catalytic phases to non-active phases [5]. While PdO decomposes to metallic Pd in the catalyst, its activity for methane conversion in the NGV applications decreases. The PdO ↔ Pd transformation is reversible, and the decomposition of PdO to Pd in the Pd/Al_2O_3 catalyst occurs at ~800 °C in air, while the re-oxidation is detected upon cooling to ~600 °C [2]. Hysteresis in the re-oxidation is due to strongly bound oxygen on the Pd surface inhibiting bulk oxidation [6]. Many factors, such as gas phase composition and pressure, affect the PdO ↔ Pd transformation [7]. For example, H_2 can reduce PdO to metallic Pd in the Pd/Al_2O_3 catalyst already at 100–150 °C, methane at 280–290 °C, and He above 700 °C [8].

Poisoning is due to the adsorption of impurities on the catalytic active sites. Poisons can also react with the active sites followed by the formation of non-active compounds [9]. In the natural gas applications, sulfur-containing compounds in the exhaust gases (originating from odorants, lubricating oils and natural gas itself) rapidly decrease the activity of the oxidation catalyst. Only a small amount of SO_2 is enough to block the active noble metal sites [3,10,11]. While SO_2 and water are present simultaneously, sulfation of the Pd/Al_2O_3 catalyst starts by oxidation of SO_2 to SO_3 on the PdO particle. After that, SO_3 over PdO can form $PdSO_4$ or migrate to the alumina support and form $Al_2(SO_4)_3$ [10,12,13]. However, sulfation is also reversible; SO_x from the catalyst surface is detected to desorb already below 400 °C and the more stable support sulfates decompose above 700 °C [13]. According to Kinnunen *et al*. [14], sulfur hinders the mobility of oxygen and desorption of water, thus decreasing the catalyst activity for methane combustion.

From the theoretical perspective, density functional theory (DFT) based calculations have been carried out to investigate the poisoning mechanism of SO_x (x=0−4) on Pd catalysts [15–18]. Using infrared reflection absorption spectroscopy (IRRAS), X-ray photoelectron spectroscopy (XPS), and DFT calculations, Luckas *et al*. reported the adsorption and reactivity of SO_2 on Pd/BaO, Pd(111) [15], and oxygen pre-covered Pd(100) surfaces [16]. The energetically preferred adsorption orientation of SO_2 on Pd(100) was the molecular plane perpendicular to the Pd surfaces, and the oxidation of SO_2 led to SO_3 and eventually to SO_4 in the presence of oxygen. Based on the *in situ* XPS and DFT calculations, the reaction kinetics of sulfur oxidation on Pd(100) has also been investigated [17], and the observed main reaction intermediates where sulfates, while the amounts of SO_2 and SO_3 were minor. More recently, Sharma *et al*. [18] have studied the SO_x (x=0−4) oxidation on the Pt(111) and Pd(111) surfaces using DFT calculations with microkinetic modeling. They concluded that the oxidation of SO_x and the formation of SO_4 species are favorable on both Pt and Pd, and that the Pd surface is more prone to sulfate formation. So far, theoretical studies have mainly focused on the interaction of SO_x with metal surfaces, and investigations of sulfur species on supported Pd nanoparticles are missing.

For practical purposes, the reactivation of the sulfur-poisoned catalysts is a very interesting topic, *e.g.*, for extending the catalyst lifetime. However, only a few scientific articles on the regeneration of sulfur-poisoned natural gas oxidation catalysts have been published. Arosio *et al*. [19] have studied the regeneration of the sulfur-poisoned Pd/Al_2O_3 catalysts by short (2 minutes) CH_4 pulses. Significant regeneration was observed already at 550 °C and almost complete reactivation of the catalyst was achieved at 600 °C. Regeneration was associated with released SO_2 due to decomposition of support sulfates promoted by CH_4 activation onto the reduced metallic Pd surface. Thus, periodical feeding of short CH_4 pulses to the NGV mufflers can regenerate the catalysts [19]. According to Kinnunen *et al*. [14], a sulfur-poisoned catalyst can be regenerated under low-oxygen conditions by decomposing $PdSO_4$ to $PdSO_3$ followed by the release of oxygen and SO_2 in a wide temperature range (800 – 1000 °C). However, decomposition of $PdSO_4$ forms metallic Pd which is an inactive phase for methane combustion [14]. Thus, scientific studies are definitely needed to understand and improve regeneration behavior of the natural gas oxidation catalysts.

In this work, sulfur deactivation and regeneration behaviors of a Pd/Al_2O_3 natural gas oxidation catalyst have been studied. Fresh and treated catalysts have been characterized by transmission electron microscopy, X-ray diffractometry, Infrared spectrometry, and their activity has been studied in catalyst performance tests. In addition, we complement the experiments by performing DFT simulations of PdO catalyst model structures on alumina support with and without interacting SO_x species.

2. EXPERIMENTAL

2.1 Catalyst material

The studied catalyst material is Pd supported on a γ-alumina washcoat on a metallic monolith. The catalyst was manufactured and designed by Dinex Ecocat Oy for lean-burn-natural-gas applications. Total palladium loading in the catalyst is 7.06 g/dm^3.

2.2 Sulfur poisoning and regeneration treatments

A sulfur with water (marked as SW) treatment was carried out at 400 °C for 5 hours in 100 ppm SO_2 + 10 % H_2O + 10 % air + N_2 bal. The gas hourly space velocity (GHSV) was 10,000 h^{-1} during the treatments. Heating to 400 °C and cooling to 25 °C were carried out under N_2 / 10 % air. A regeneration after the SW treatment (marked as Reg. CH_4) was carried out at 600 °C for 30 minutes in 1 % CH_4 + N_2 bal. Heat treatments for the regenerated (marked as Reg. CH_4+Reg. O_2) catalyst were carried out at 200 – 600 °C for 30 minutes in air.

2.3 Characterization

The fresh, SW-treated, and regenerated catalyst samples were studied by field emission scanning electron microscopy (FESEM, Zeiss, Crossbeam 540) together with energy dispersive spectroscopy (EDS, Oxford Instruments, 80 mm^2 XMax^N silicon-drift detector) to determine the distribution and amount of sulfur. In addition, backscattered electron (BSE) images by an energy selective backscattered (EsB) detector were collected. The cross-sectional samples for FESEM studies were prepared with a conventional metallographic method: molding to resin, grinding and polishing followed by carbon-coating to avoid the sample charging in the FESEM studies. The structure of the catalysts was studied by transmission electron microscopy (TEM) and X-ray diffractometry (XRD). A TEM (Jeol JEM-2010) was used for imaging. A high resolution (scanning) TEM (HR(S)TEM, Jeol 2200FS) with two aberration correctors (CEOS GmbH) was used for high resolution STEM imaging. Bright-field (BF) and dark-field (DF) STEM images were collected. The Pd particle diameter for the fresh, SW-treated, and regenerated catalyst samples were measured from the DF STEM images. Over 50 particles were measured. The catalyst samples for all TEM studies were prepared by crushing the scraped catalyst powder between two laboratory glass slides and dispersing the crushed powder with ethanol onto a copper grid with a holey carbon film. The scraped catalyst powder was also used for XRD (PANanalytical, Empyrean with the PIXcel^{3D} detector, using Cu Kα radiation with a wavelength 0.15418 nm) studies. Phases were identified

from XRD patterns by using the database (PDF-4+ 2016) from the International Centre for Diffraction Data (ICDD) and crystallite sizes were determined with the aid of the HighScore plus software based on the Scherrer equation (shape factor 0.9).

Specific surface areas, pore sizes, and pore volumes of the fresh and treated catalysts were determined using the Micrometrics ASAP 2020. Specific surface areas were measured from the N_2 adsorption isotherms at -196 °C (77 K) according to the standard BET (Brunauer-Emmett-Teller) method. Pore size and pore volume distributions of catalysts were calculated from N_2 desorption isotherms by the BJH (Barrett–Joyner–Halenda) method.

A Fourier transform infrared (FT-IR) spectrometer (Bruker Vertex V80) equipped with a diffuse reflectance infrared Fourier transform (DRIFT) unit and a liquid nitrogen-cooled mercury cadmium telluride (MCT) detector was utilized to find the information about the bonding of the sulfur compounds on the scraped catalyst powder. The DRIFT analyses were performed at room temperature under ambient atmosphere conditions. The background spectrum was measured using a mirror. Spectra were recorded by using a resolution of 4 cm^{-1}.

2.4 Catalytic testing

Laboratory scale light-off tests were used to determine the catalyst activity of the fresh and treated catalysts. Catalytic activities were determined in lean reaction conditions using the following gas mixture: 600 ppm CH_4, 500 ppm CO, 10 vol% CO_2, 12 vol% O_2, 10 vol% H_2O, and N_2 as balance gas. The total gas flow was 1 $dm^3.min^{-1}$ resulting in a GHSV of 31000 h^{-1}. The measurements were carried out at atmospheric pressure in a horizontally aligned tubular quartz reactor. The temperature of the catalyst bed was increased from room temperature up to 600 °C with a linear heating rate of 10 °C.min^{-1}. The reactor was first heated up to 100 °C under N_2 flow and then the gas mixture and water was inserted to the reactor. The catalyst was kept at steady state for 15 min at 600 °C and after that the reactor was cooled down to room temperature under the N_2 flow. Gas flow rates were controlled by using mass flow controllers (Brooks 5280S). The gas composition was analyzed as a function of temperature by a Gasmet^{TM} FT-IR gas analyzer. Oxygen concentration was determined by using a paramagnetic oxygen analyzer (ABB Advanced Optima).

2.5 Catalyst modeling

Spin-polarized density functional theory (DFT) calculations were carried out by using the CP2K program package [20,21] for all the model systems reported herein. The gradient-corrected functional of Perdew,

Burke and Ernzerhof (PBE) [22] and the analytic pseudopotentials of Goedecker, Teter, and Hutter (GTH) [23] were employed in the calculations. Gaussian basis sets of double-zeta valence polarized (DZVP) [24] were adopted to expand the wave functions, while the cutoff energy of the auxiliary plane-wave basis for electron density was set at 600 Ry [25]. The Γ-point approximation was employed for Brillouin zone integration as the model systems are laterally large and the alumina substrate (slab) is an insulator. The DFT-D2 method was used to account for the weak van der Waals interactions [26]. Bader analysis of effective charges of atoms (based on electron density) was used to determine the charge transfer [27,28]. The activation energy barriers were calculated using the climbing-image nudged elastic band (CI-NEB) method [29].

The slab models of the alumina (100) surface used as the support were cleaved from a non-spinel γ-Al_2O_3 model [30]. The slab model consists of 4×3 unit cells in laterally and four layers normal to the surface (480 atoms, 22.33×25.19 $Å^2$). To avoid lateral interactions of periodic catalyst replica, a larger slab with 5×3 unit cells laterally (600 atoms, 27.92×25.19 $Å^2$) is also employed when more SO_x species are adsorbed on the catalyst. A Pd_{30} cluster with the square-base pyramidal structure is considered as the model structure for the Pd catalyst. The corresponding PdO catalyst cluster follows the internal geometry of bulk PdO, while the surface is sufficiently covered by oxygen atoms; the stoichiometry of the PdO model catalyst is $Pd_{30}O_{44}$. Note that the Pd sublattice is the same as for Pd_{30} (fcc). In this study, the catalyst of the $Pd_{30}O_{44}$ cluster on the Al_2O_3 substrate is considered as a representative model. A larger model catalyst would need a much larger substrate to ensure no cluster-cluster interactions. This would result in several thousands of atoms in the model structure and such DFT-simulations are not feasible in this context.

3 RESULTS AND DISCUSSION

3.1 Fresh catalyst

The cross-sectional FESEM (BSE) image of the catalyst material, Pd supported on the γ- Al_2O_3 washcoat, on the metallic monolith is presented in Fig. 1a. The size of the Pd particles is too small to be detected by FESEM. According to the TEM (Fig. 1b−d) and XRD (Fig. 2) results as well as S_{BET} and BJH values (Table 1), the fresh catalyst has a nanocrystalline and porous γ-Al_2O_3 support with well-distributed PdO crystallites. The crystallite size of PdO in the fresh catalyst is 2 nm measured from the XRD pattern based on the Scherrer equation. The average diameter of the PdO particles was 1.8 ± 0.5 nm measured from the DF STEM images, the histogram is presented in Fig. 3a. According to the BF STEM images (Fig. 1d), the PdO particles are single crystals and the crystallite size measured by XRD and the particle size measured from STEM images correspond to each other. The model catalyst structure of a $Pd_{30}O_{44}$ cluster on γ-

Al_2O_3(100) has been optimized by DFT (Fig. 1e). Upon optimization, the $Pd_{30}O_{44}$ cluster exhibits a hemisphere-like overall shape with the base diameter of 10.96 Å and the height of 7.18 Å. The nearest Pd-O bond length varies in the range of 1.97−2.09 Å, which is comparable to the bulk value 2.02 Å. The optimized bond distances between the cluster and the support surface vary between 1.85−2.21 Å. The calculated cluster adsorption energy (E_{ads}^1) of $Pd_{30}O_{44}$ is 17.46 eV (0.185 eV/Å^2). Here, E_{ads}^1 is defined as

$$E_{ads}^1 = E(Pd_{30}O_{44}) + E(Al_2O_3) - E(Pd_{30}O_{44}/Al_2O_3) \quad (1)$$

where *E(X)* is the total energy of the related system *X*. The Bader charge analysis reveals that the $Pd_{30}O_{44}$ cluster gains 4.12*e* of electron density in total, originating from the Al_2O_3 substrate, which results in that the negatively charged catalyst is prone to interact with adsorbate molecules. The catalyst model structure of a Pd_{30} cluster on γ-Al_2O_3(100) is also optimized and shown in the Supporting Information (Fig. S1). The pyramid-like geometry has a base dimension of 8.03 × 7.98 Å^2 and height of 5.50 Å. The bond distances between the cluster and support surface vary between 2.01−2.25 Å. The calculated adsorption energy of the Pd_{30} cluster on γ-Al_2O_3(100) is 12.80 eV (0.200 eV/Å^2), and according to the Bader analysis, the support donates 1.62*e* of electron density to the cluster.

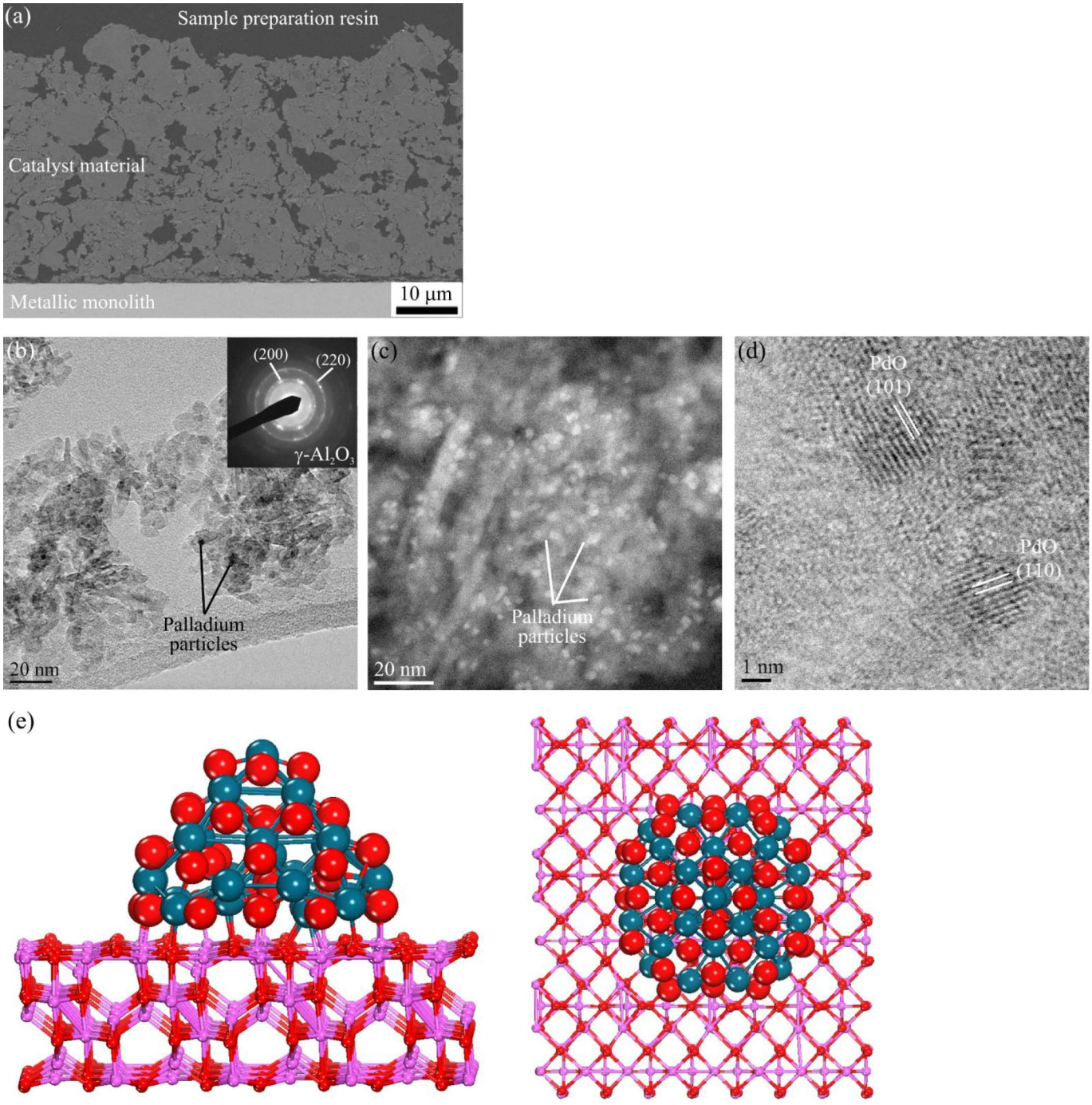

Figure 1. *The fresh catalyst, (a) the cross-sectional FESEM (BSE) image showing the structure of the catalyst monolith, (b) the TEM image with the selected area electron diffraction (SAED) pattern and (c) the DF STEM image both indicating uniformly distributed palladium particles and nanocrystalline γ-Al_2O_3, (d) BF STEM image of the palladium particles wherein lattice fringes correspond to PdO, and (e) DFT-optimized model structure (side-view and top-view) of a PdO cluster catalyst on γ-Al_2O_3 (color key: Pd, dark green; O, red; Al, pink).*

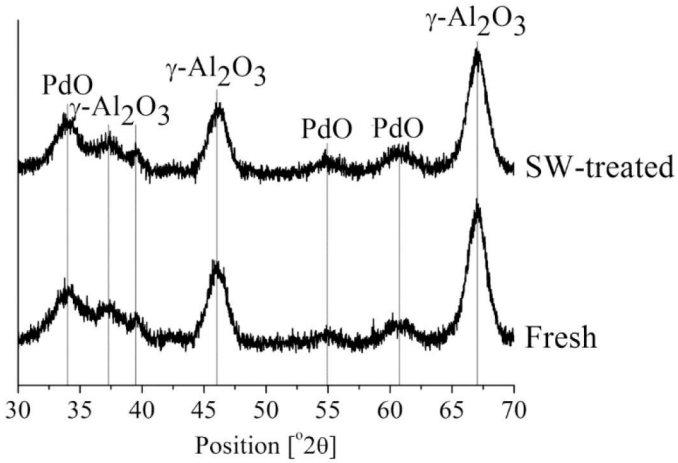

Figure 2. *XRD patterns for the fresh and SW-treated catalysts.*

Table 1. *Specific surface area (S_{BET}), total pore volume, and average pore size of the fresh, SW-treated and regenerated (in CH_4 conditions after SW-treatment) catalysts.*

Catalyst	Specific surface area [m^2/g]	Total pore volume [cm^3/g]	Average pore size [nm]
Fresh	180	0.38	8.5
SW-treated	175	0.34	8.0
Reg. CH_4	184	0.40	8.6

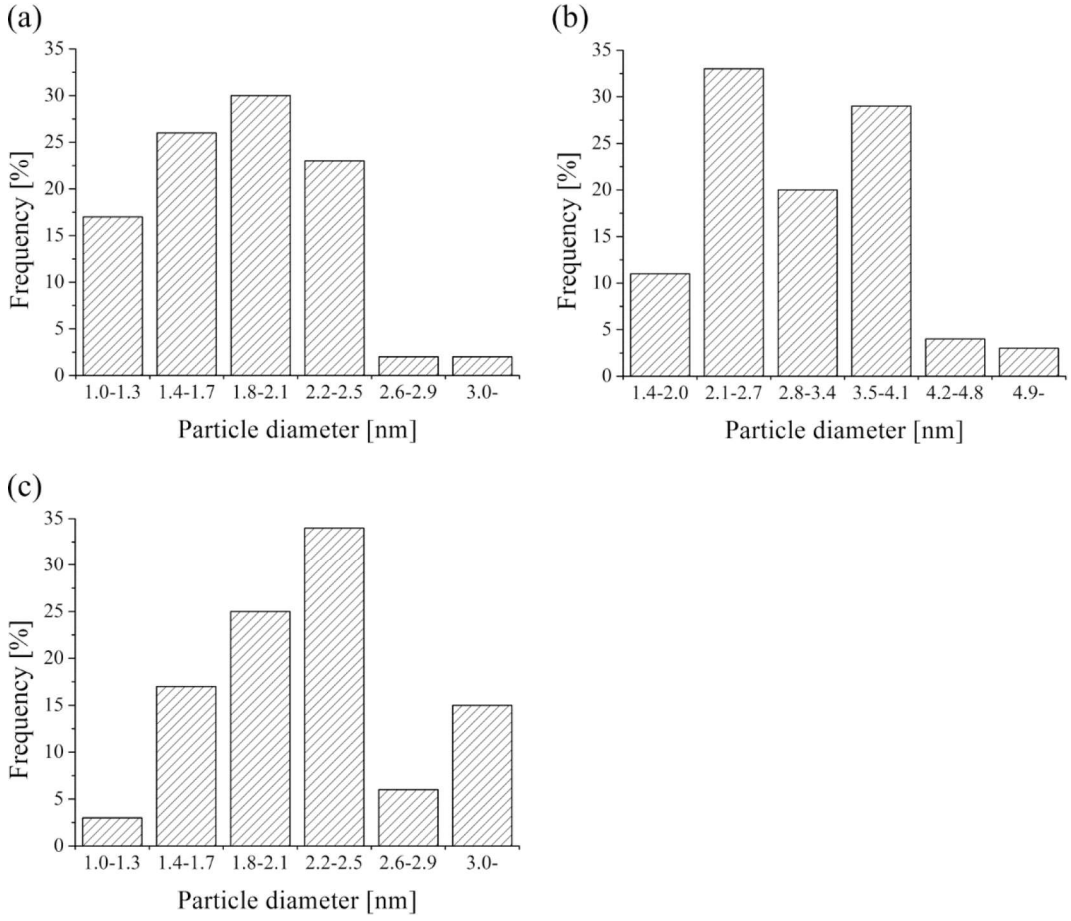

Figure 3. *Particle size distribution histograms of (a) the fresh catalyst, (b) the SW-treated catalyst, and (c) the regenerated (in CH_4 conditions after SW-treatment) catalyst.*

To understand the chemical nature of the $Pd_{30}O_{44}$ cluster adsorption on Al_2O_3, the projected density of states (PDOS) of electronic structure, charge density difference (CDD) and HOMO-LUMO orbitals are visualized in Fig. 4. PDOS (Fig. 4a) shows the projection of Kohn-Sham single-particle states onto atomic *s*-, *p*- and *d*-components in the catalyst and support, respectively. At the Fermi energy, PDOS has significant weight on the catalyst, while the support (insulator) displays a band gap. The corresponding electronic states have predominant contributions from the atomic *p*- (oxygen) and *d*-orbitals (palladium) in the $Pd_{30}O_{44}$ cluster. Especially, the metallic *d*-contribution at the Fermi level is a promising indicator for the interaction with reactant molecules and catalytic activity. From the CDD visualization (Fig. 4b), one can observe significant charge accumulation and depletion at the interface between the $Pd_{30}O_{44}$ cluster and Al_2O_3 substrate, in agreement with the observed pronounced charge transfer between the cluster and substrate. In particular, the accumulated charge is distributed around the cluster perimeter. Furthermore, the HOMO and LUMO orbital distributions (Fig. 4b) show that both states are mainly delocalized around the $Pd_{30}O_{44}$ cluster (supporting the PDOS results in Fig. 4a), while there is insignificant electron distribution around the Al_2O_3 support. Similar observations were made for the non-oxidized Pd_{30} cluster catalyst on Al_2O_3, and the corresponding PDOS, CDD visualization and HOMO-LUMO orbitals are given in Fig. S2.

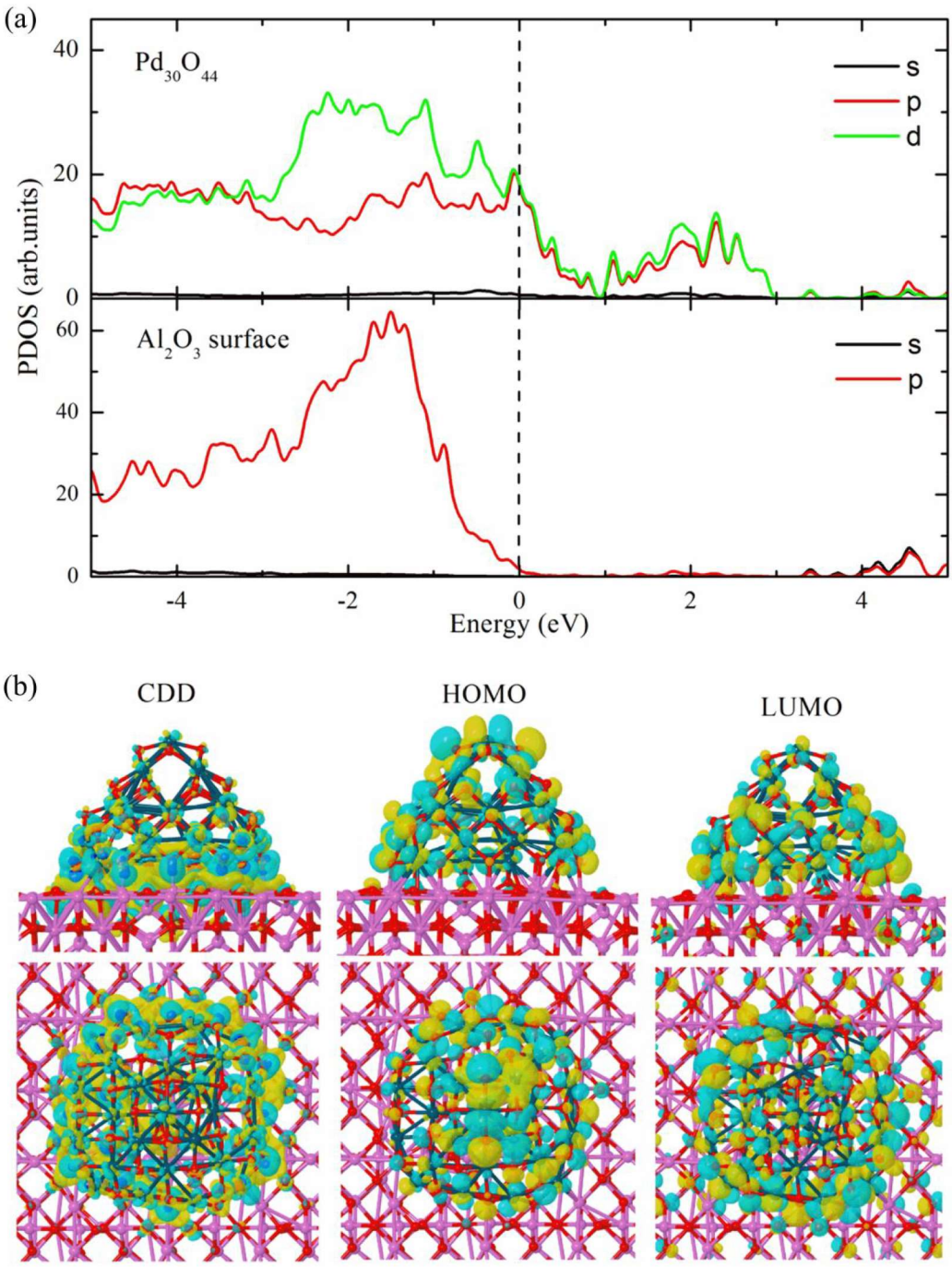

Figure 4. *Calculated electronic properties of the $Pd_{30}O_{44}/Al_2O_3(100)$ system: (a) Projected density of states (PDOS) onto atomic s-, p- and d- orbitals in the cluster and support, respectively. The vertical dashed line indicates the Fermi level, where the main weight can be associated with O-2p and Pd-4d. (b) Side and top views of charge density difference (CDD) and HOMO/LUMO orbitals. For CDD, the yellow and cyan colors represent charge accumulation and depletion, respectively, while the net accumulation in the cluster is 4.12 e. For HOMO/LUMO, the different colors mark different nodes (signs) of the corresponding wavefunction. The isosurface values are $\pm 0.002\ e/a_0^3$ for CDD and $\pm 0.01\ e/a_0^3$ for HOMO and LUMO.*

3.2 SW-treated catalyst

Based on the XRD (Fig. 2) and TEM (Fig. 5) results, the morphology of the γ-Al_2O_3 support after the SW-treatment is similar to the fresh catalyst. In addition, palladium particles were detected in the PdO form after the SW-treatment (Figs. 2 and 5c), similar to the fresh catalyst. However, the PdO crystallite size in the SW-treated catalyst is 4 nm as measured from the XRD pattern (Fig. 2) by the Scherrer equation while it was 2 nm in the fresh catalyst. The average diameter of the PdO particles was 3.0 ± 0.8 nm measured from the DF STEM images, the histogram is presented in Fig. 3b. According to the BF STEM images (Fig. 5c), the PdO particles are single crystals. There is a slight fluctuation between the measurements by XRD and from the STEM images likely due to a small sampling of the particles in the measurement from the STEM images. However according to both measurements, a slight crystallite growth of PdO occurred during the SW-treatment. Lee *et al*. [31] have proposed that SO_2-induced sintering of Pt particles in the Pt/Al_2O_3 catalyst results from the reaction of SO_2 with oxygen at the Pt-O-Al interface weakening the Pt–O interaction and promoting the migration and sintering of Pt particles. A similar mechanism may cause a slight sintering of PdO crystallites in the studied catalyst. According to our earlier study [32], a slight sulfur-induced growth of the PtPd particles in the PtPd/Al_2O_3 catalyst was observed and a small amount of bulk aluminum sulfate species was detected near the PtPd particles. In the studied catalyst, the micro-scale distribution of sulfur studied by FESEM-EDS was observed to be uniform and the amount of sulfur was ~2 wt%. According to the DRIFT spectra (Fig. 6), at 1160−1200 cm^{-1} the formation of bulk $Al_2(SO_4)_3$ on the SW-treated catalyst was detected [33,34]. However, the band at ~1300 cm^{-1} indicating surface $Al_2(SO_4)_3$ [33] was not observed. Also, the band at ~1435 cm^{-1} corresponding to ν(S=O) of Pd−SO_4 species [35] was not found. It can be assumed that the bands at 1035 and 1639 cm^{-1} are material originated ones as they exist in all spectra and their intensities and band positions were not changed or affected by treatments. It has been reported that the sulfur poisoning of the Pd/Al_2O_3 catalyst starts by oxidation of SO_2 to SO_3 on the PdO particle followed by the formation of $PdSO_4$ and/or $Al_2(SO_4)_3$ [10,12,13]. Based on these results, it can be deduced that sulfur migrates to the Al_2O_3-based support forming bulk $Al_2(SO_4)_3$. Sulfur compounds likely block a part of the pore openings resulting in a slightly decreased specific surface area, total pore volume, and average pore size during the SW-treatment (Table 1).

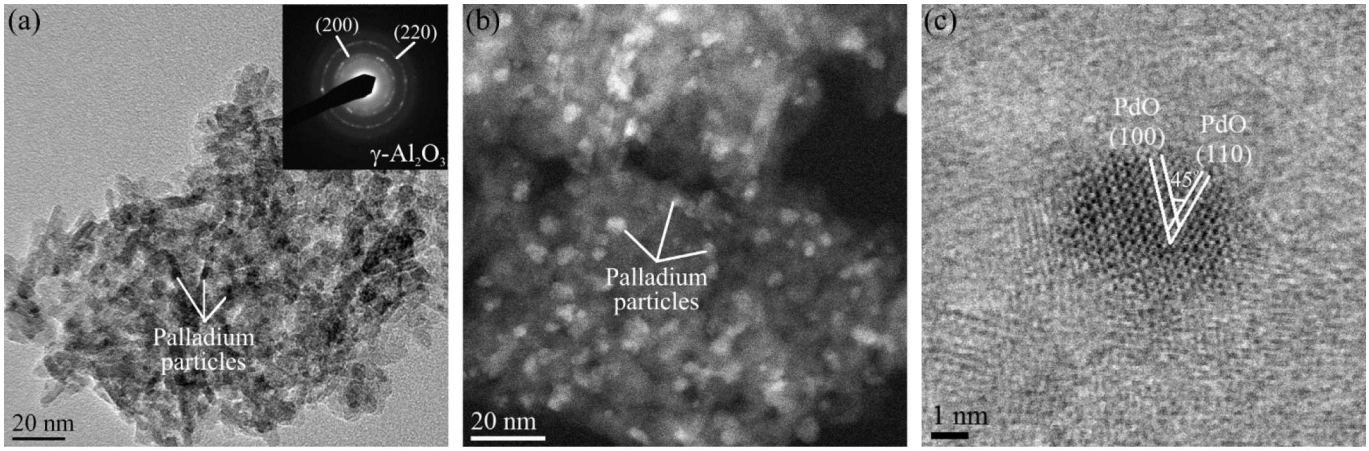

Figure 5. *The SW-treated catalyst, (a) the TEM image with the SAED pattern and (b) the DF STEM image both indicating uniformly distributed palladium particles and nanocrystalline γ-Al_2O_3 and (c) the BF STEM image of the palladium particle wherein lattice fringes correspond to PdO.*

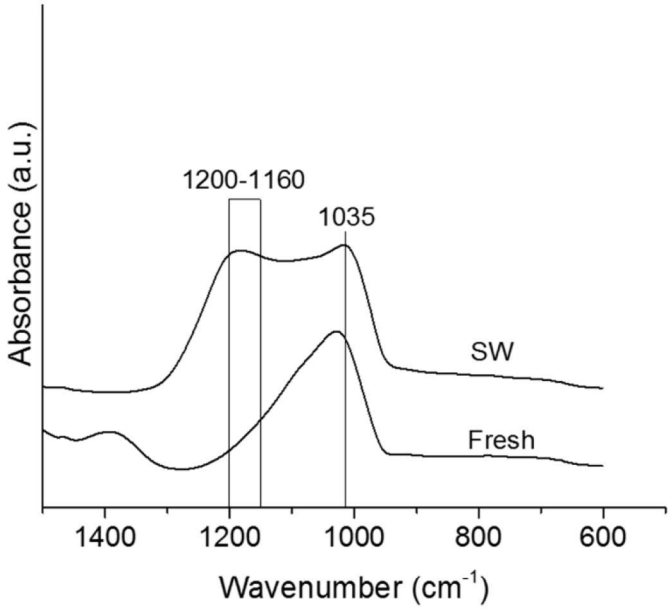

Figure 6. *DRIFT spectra for the fresh and SW-treated catalysts.*

Since the sulfur oxides (SO_x) will modify the catalyst surface chemistry and prevent access of reactants to the surface, it is necessary to identify and get detailed knowledge on the adsorption properties of the SO_x species on the $Pd_{30}O_{44}/Al_2O_3$ catalyst and estimate the saturation adsorption of SO_x. The optimized most stable structures of a single SO_x adsorption on the $Pd_{30}O_{44}/Al_2O_3$ catalyst are shown in Fig. S3. The calculated adsorption energy (E_{ads}^{SOx}), net charge and geometric parameters are summarized in Table S1. According to DFT optimizations, the adsorbed SO_x forms the following configurations: SO_2 for S, SO_3 for SO, and SO_4 for SO_2 and SO_3, respectively, through binding more O atoms from the PdO cluster surface. This is in agreement with the experimental observations, where stable configurations of SO_2, and then SO_3 and SO_4 have been observed upon SO_x adsorption on Pd catalysts in the presence of oxygen [15–17]. The SO_x (x=0-4) species show a strong interaction with the catalyst due to covalent binding where the adsorbed SO has the largest adsorption energy. Bader charge analysis shows that PdO donates

electron density towards SO_x. Overall, the amount of charge transfer increases almost linearly with *x*, and an adsorbed SO_4 gains 0.72*e* additional charge from PdO.

As a representative case, the saturation adsorption of SO_3 on $Pd_{30}O_{44}/Al_2O_3$ has been carefully evaluated by adding SO_3 molecules one-by-one on the catalyst. The adsorption energy of the *n*-th SO_3 molecule ($E_{ads}^{(SO3)n}$) was calculated as:

$$E_{ads}^{(SO3)n} = E(SO_3) + E(n\text{-}1) - E(n) \quad (3)$$

where $E(SO_3)$, $E(n\text{-}1)$ and $E(n)$ are the total energies of the SO_3 molecule and systems with (*n*-1) and *n* adsorbed SO_3. The calculated $E_{ads}^{(SO3)n}$ as a function of SO_3 number *n* is plotted in Fig. 7a. The $E_{ads}^{(SO3)n}$ varies in the range of 0.50 (n = 5) to 2.22 eV (n = 15) for n=1-16, and then goes to a negative value at n=17 (Fig. 7a). Thus, the saturation adsorption of $(SO_3)_n$ on $Pd_{30}O_{44}/Al_2O_3$ is reached at *n*=16, corresponding to a case where $Pd_{30}O_{44}$ is encapsulated by SO_x (Fig. 7c). Despite the forming S-O bonds, the catalyst structure retains the original internal Pd-O geometry. It was observed also by STEM that the structure of the PdO particles is similar in the fresh and SW-treated catalysts (Figs. 1d and 5c). All adsorbed SO_3 molecules form $PdSO_4$ complexes by binding Pd and O atoms on the $Pd_{30}O_{44}$ surface, while the SO_3 at the interface also bind Al atoms in the Al_2O_3 support. The average adsorption energy of a SO_3 molecule is 1.01 eV. The PDOS of the SO_3 encapsulated (*n*=16) case is displayed in Fig. 7b. Although there is still considerable weight, the features near the Fermi level have changed in comparison with the naked $Pd_{30}O_{44}$ cluster due to the covalent bonding between sulfur and oxygen. Bader charge analysis shows that the PdO cluster donates 4.69*e* of electron density to the encapsulating layer, leaving the cluster itself slightly negatively charged followed by reduction in chemical activity (see below).

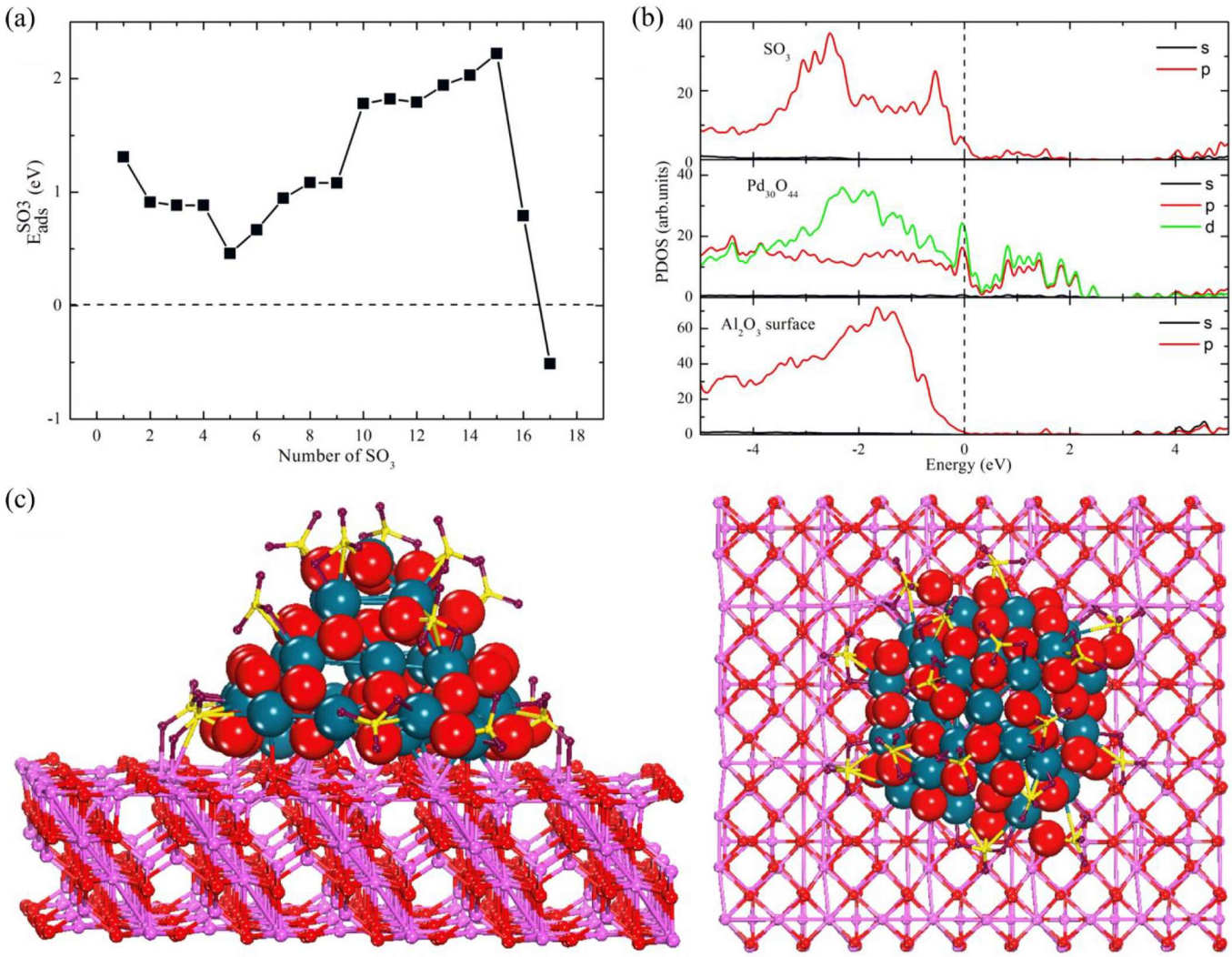

Figure 7. *(a) SO_3 adsorption energy ($E_{ads}^{(SO3)n}$) as a function of SO_3 number n for multiple SO_3 adsorbed on $Pd_{30}O_{44}/Al_2O_3(100)$. (b) Projected density of states (PDOS) onto atomic s-, p- and d-orbitals for $(SO_3)_{16}$ adsorbed $Pd_{30}O_{44}/Al_2O_3(100)$. The vertical line indicates the Fermi level. (c) Side and top view of the optimized structure of $(SO_3)_{16}$ adsorbed $Pd_{30}O_{44}/Al_2O_3(100)$. The Pd-sublattice remains intact.*

Experimentally, sulfur composition has been observed also within the interior of the PdO catalysts upon SO_x exposure. Correspondingly, we have probed the substitution of O atoms by S atoms inside the $Pd_{30}O_{44}/Al_2O_3$ catalyst. At first, the diffusion of O and S atoms from the surface towards the interior of the Pd_{30}/Al_2O_3 catalyst has been simulated. The optimized structures and energy diagrams along the diffusion paths are given in Fig. S5 and S6. The diffusion barriers for sulfur are lower, 0.86 (first transition state, TS1) and 1.02 eV (second, transition state, TS2), than those for oxygen, 0.94 (TS1) and 1.17 eV (TS2). Based on these results, we estimate that atomic sulfur diffuses more readily inside fresh Pd catalysts than oxygen.

For the substitution of O atoms in the $Pd_{30}O_{44}$ cluster, the optimal sulfur substitution site was found at the bottom layer of $Pd_{30}O_{44}$, where the substituted S atom is tetrahedrally surrounded by four Pd atoms with the S-Pd bond lengths of 2.4 Å (compare with that of 2.1 Å for O-Pd). The S substitution is energetically

favorable by 0.67 eV. Here, the substitution energy was calculated as the difference between the total energies of individual systems before substitution (free S atom and PdO catalyst) and those of after substitution (free O atom and S-substituted PdO catalyst). The number of substituting S atoms has also been varied between 2 and 6 in the bottom layer of the PdO cluster. The calculated substitution energies are 0.61 and 0.51 eV/S, respectively, while PDOS does not show significant changes (Fig. S7). The longer Pd-S bond distances cause strain inside the cluster and one cannot increase the S-content further without breaking the internal geometry of the cluster. Overall, the direct substitution by S inside the cluster does not give indications of reduced catalytic activity, while there are geometric limitations in terms of strain.

3.3 Regenerated catalysts

Based on the XRD (Fig. 8a) and TEM (Fig. 9a) studies, the morphology of the γ-Al_2O_3 support in the regenerated (in CH_4 conditions after SW-treatment) catalyst is similar to the fresh and SW-treated catalysts. However, during the regeneration treatment, PdO particles have partly reduced to metallic Pd (Figs. 8a and 9c). The crystallite size of Pd cannot be determined based on the XRD pattern due to the overlapping of the Pd and γ-Al_2O_3 peaks. The average diameter of the Pd particles was 2.3 ± 0.7 nm measured from the DF STEM images thus the size of Pd particles is similar to the size of the PdO particles in the fresh (Fig. 1) and SW-treated (Fig. 5) catalysts. According to the DF STEM images (Fig. 9b), the Pd particles are uniformly distributed and based on the BF STEM images (Fig. 9c), the particles are single crystals. Based on the literature, methane can reduce PdO in the Pd/Al_2O_3 catalyst already at 280–290 °C [8]. In our study after the regeneration treatment in CH_4 conditions, a small amount of sulfur (~1 wt%) was still detected by FESEM-EDS uniformly in the catalyst layer. In the DRIFT spectrum of the regenerated catalyst (Fig. 8b), a band at 1194 cm^{-1} was detected indicating bulk $Al_2(SO_4)_3$ [33,34]. In addition, a band at 1468 cm^{-1} assigned to sulfur species on the palladium particles [36,37] was detected, although this was absent after the SW treatment (Fig. 8b). This could be due to SO_3 spilling from the support onto PdO forming $PdSO_4$ [10]. Gélin *et al*. [38] have suggested that when sulfate species are only partly removed from the catalyst, sulfates can migrate back and forth between PdO and the Al_2O_3 support preventing the complete regeneration until there is no sulfur species in the neighborhood of PdO particles. In addition, the decomposition of $PdSO_4$ to $PdSO_3$ releases oxygen and SO_2 and forms metallic Pd [14]. Partial reduction of PdO to Pd was observed by XRD (Fig. 8a) during the regeneration treatment with methane in this study. The S_{BET} and BJH values after the regeneration recovered to the level of the fresh catalyst (Table 1) most probably indicating the removal of bulk $Al_2(SO_4)_3$ from pore openings.

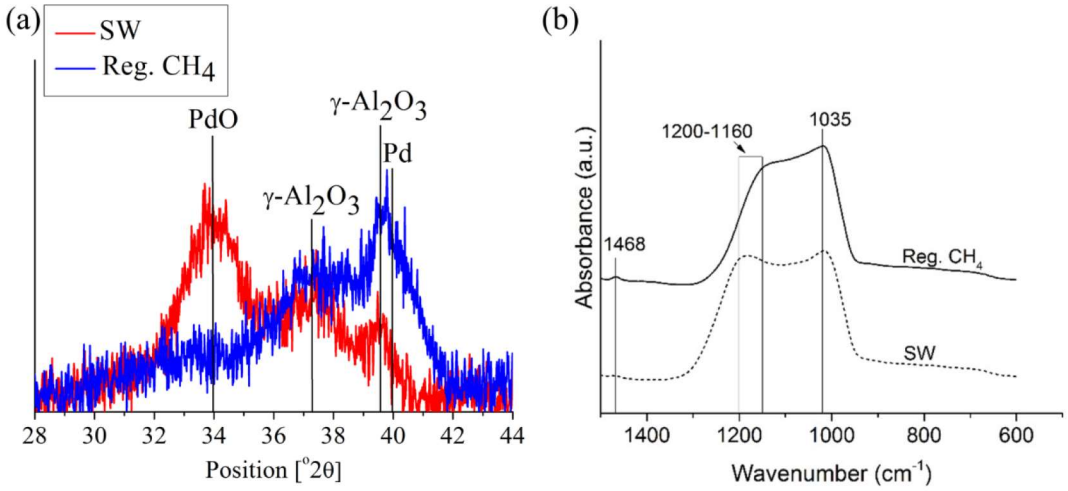

Figure 8. *(a) XRD patterns and (b) DRIFT spectra for the catalyst after the regeneration treatment in CH_4 conditions. The SW-treated catalyst is presented for comparison.*

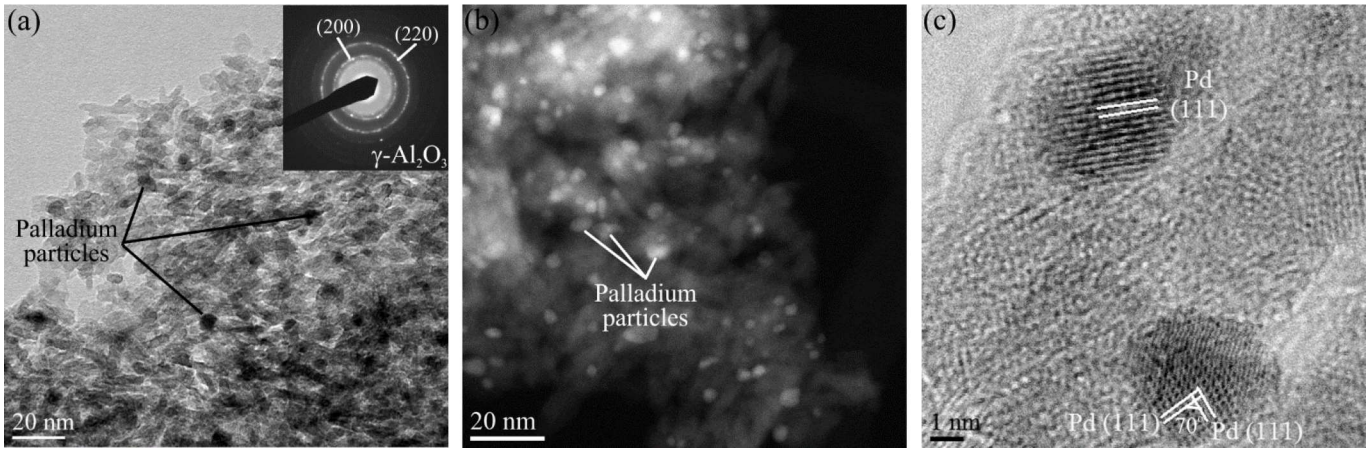

Figure 9. *The regenerated (in CH_4 conditions after SW-treatment) catalyst, (a) the TEM image with the SAED pattern and (b) the DF STEM image both indicating uniformly distributed palladium particles and nanocrystalline γ-Al_2O_3 and (c) BF STEM image of the palladium particles wherein lattice fringes correspond to metallic Pd.*

To study how Pd can be reoxidized to PdO after the regeneration treatment and to study the effect of Pd vs. PdO on the catalyst performance, the regenerated (in CH_4 conditions) catalyst was further regenerated in O_2 conditions at various temperatures. According to the XRD results (Fig. 10a), reoxidation started at 300 °C (PdO peaks started to grow) and the XRD pattern of the catalyst treated at 350 °C was similar to the XRD pattern of the fresh catalyst indicating complete oxidation. When Pd reoxidizes to PdO, the color of the catalyst changes from black back to light brown similar to the fresh catalyst (Fig. 10a). The DRIFT measurements of the further regenerated (in O_2 conditions) catalysts (Fig. 10b) still show the presence of bulk $Al_2(SO_4)_3$ (bands at 1160−1200 cm^{-1}) at all studied temperatures (200−600 °C). Also, the FESEM-EDS studies indicated a small amount (~1 wt%) of sulfur uniformly distributed in the catalyst. A band at 1468 cm^{-1} (Fig. 10b), indicating sulfur species on the palladium particles [36,37], disappears at higher temperatures. The unassigned band at 1560 cm^{-1} was found to follow the same trend. The most probable explanation is that sulfur species decompose in the neighborhood of the palladium

particles more efficiently at higher temperatures and thus, after the 30 minutes treatment at higher temperatures only bulk $Al_2(SO_4)_3$ exists. The gained results are in agreement with the results by Arosio *et al*. [19].

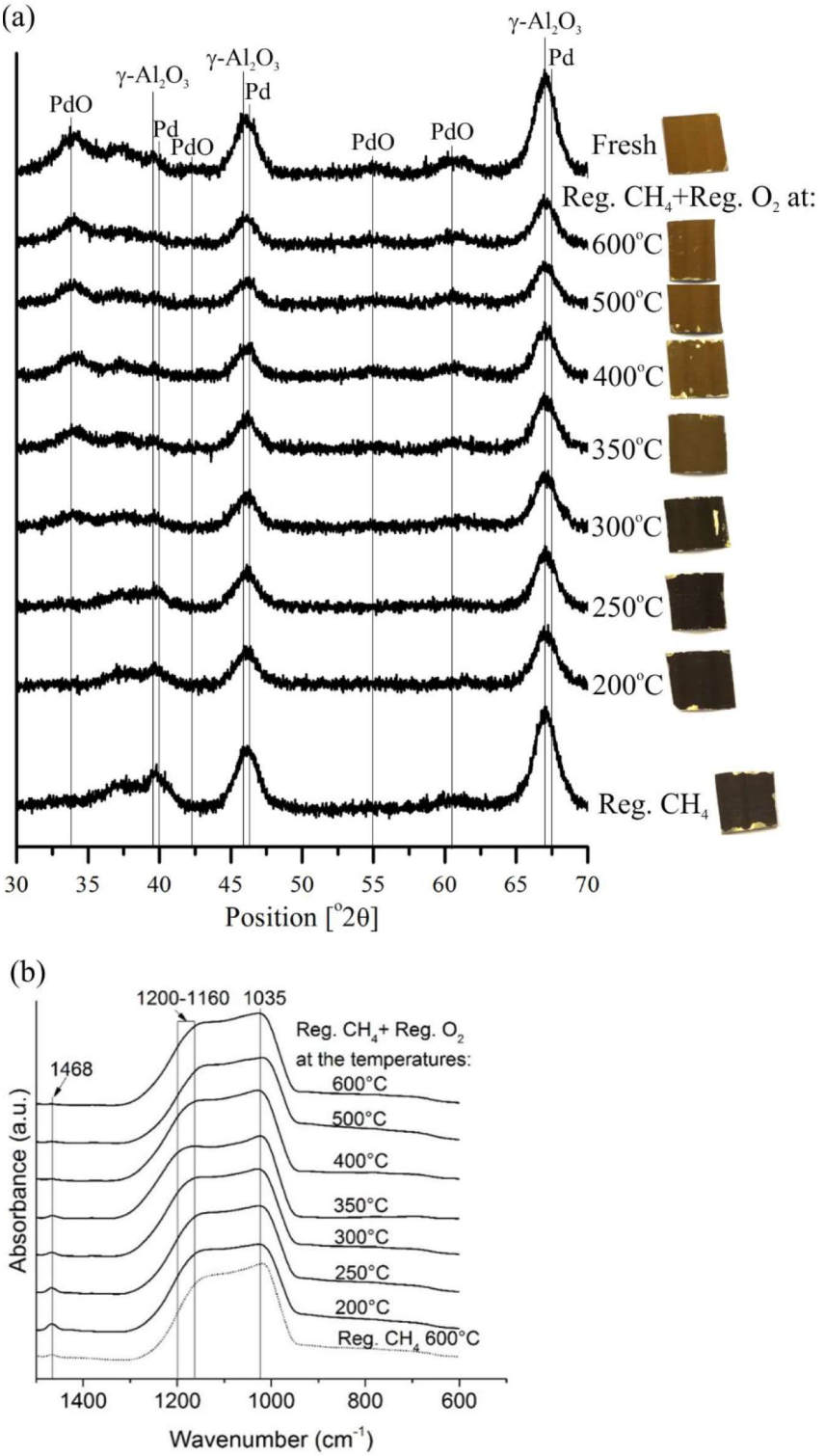

Figure 10. *(a) XRD patterns for the catalysts after the regeneration treatment in CH_4 conditions followed by the regeneration treatment in O_2 conditions at 200–600 °C. The XRD patterns for the catalyst after regeneration treatment in CH_4 conditions and the fresh catalyst are presented for comparison. In addition, the pictures of the corresponding catalyst monoliths are presented showing their color. (b) DRIFT spectra for the catalysts after the regeneration treatment in CH_4 conditions followed by the regeneration treatment in O_2 conditions at 200–600 °C.*

3.4 Catalyst performance in CH_4 oxidation

The performance of the catalysts in CH_4 oxidation was studied theoretically and experimentally. The first C-H bond activation upon CH_4 oxidation ($CH_4 + O^* + O^* \rightarrow CH_3O^* + OH^*$) was simulated on the $Pd_{30}O_{44}/Al_2O_3$ system since the first C-H bond activation is the crucial step for the rest C-H bonds breaking in CH_4 [39]. The optimal adsorption site of the CH_4 molecule was mapped by placing CH_4 on different sites on the $Pd_{30}O_{44}$ surface. Based on the preferable CH_4 adsorption site, a co-adsorption configuration of CH_3+H was also optimized. Here, the adsorption energy (E_{ads}^2) was calculated as

$$E_{ads}^2 = E(adsorbate) + E(Pd_{30}O_{44}/Al_2O_3) - E(adsorbate + Pd_{30}O_{44}/Al_2O_3) \quad (2)$$

where E(X) is the total energy of the corresponding system X. Figure 11 displays the structures of the initial state (IS), transition state (TS), intermediate state (IM), and final state (FS), and the energy diagram of reaction pathway for the first C-H bond activation in CH_4 oxidation over O*-O* site pairs (labeled with O_1-O_2), respectively. At IS, the CH_4 molecule binds weakly on the $Pd_{30}O_{44}$ surface with E_{ads}^2 = 0.40 eV and the C-Pd distance of 3.25 Å. Note that the binding site is at the cluster-surface perimeter which is also the region of most donated charge (Fig. 4). In the first transition state (TS1), the C-H bond length increases from 1.10 Å (CH_4 in gas phase) to 1.33 Å and binds to the Pd and O* (labeled O_1) atoms with the C-Pd, H-Pd and H-O* bond lengths of 2.25, 1.86 and 1.31 Å, respectively. The corresponding activation barrier is 0.66 eV, consistent with the scaling of 0.76 ± 0.11 eV computed by the methane C-H bond activation equation in Ref. [40]. The elongated C-H bond in TS1 cleaves as the reaction progresses leading to the formation of C-Pd and H-O* bonds at IM. After that, the CH_3O^* + HO* fragments are produced at FS after crossing over the second transition state (TS2) with a reaction barrier of 0.43 eV along the reaction path. For reference, the first C-H bond activation upon CH_4 dissociation over a pyramidal Pd_{30} cluster supported on γ-Al_2O_3(100) surface was also simulated (Fig. S4), and the resulting activation barrier (0.88 eV) is noticeably higher than that of the PdO catalyst. This is agreement with the general knowledge that PdO is more active in CH_4 oxidation than Pd. Similar transition states have also been observed for CH_4 activation over PdO(101) and Pd(111) surfaces with the calculated activation barriers of 0.64 and 0.76 eV, respectively [41].

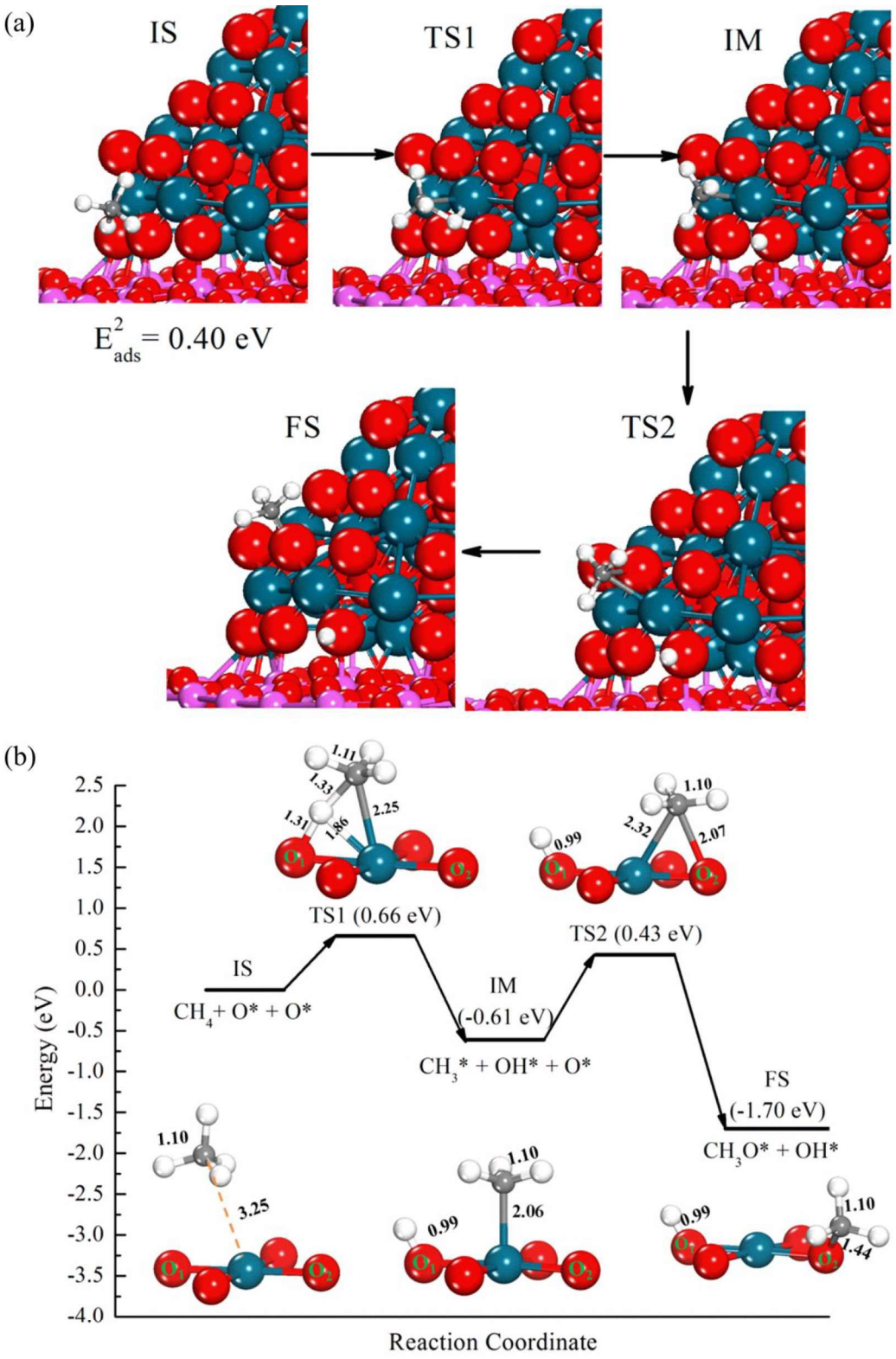

Figure 11. *CH_4 oxidation (CH_4 + O* + O* → CH_3O* + OH*) on the $Pd_{30}O_{44}/Al_2O_3(100)$ catalyst: (a) Structures of the initial state (IS), transition state (TS), intermediate state (IM), and final state (FS). (b) Energy diagram of the reaction pathway on O*-O* site pairs (labeled with O_1-O_2). Color code: H, white; C, gray; O, red; and Pd, dark green.*

During the SW-treatment, the methane oxidation performance of the catalyst decreased significantly compared to the fresh catalyst (Table 2 and Fig. 12). Formed bulk $Al_2(SO_3)_4$ and the slight growing of the PdO crystallites likely decreased the activity of the SW-treated catalyst.

Table 2. *Light-off temperatures (T_{50} and T_{90} are temperatures at which the CH4 conversion is 50 % and 90 %, respectively) for CH_4 oxidation over the fresh, SW-treated and regenerated (Reg. CH_4 and Reg. CH_4 +Reg. O_2 (500 °C)) catalysts.*

Catalyst	T_{50} [°C]	T_{90} [°C]
Fresh	347	412
SW-treated	448	527
Reg. CH_4	375	461
Reg. CH_4 + Reg. O_2 (500 °C)	386	455

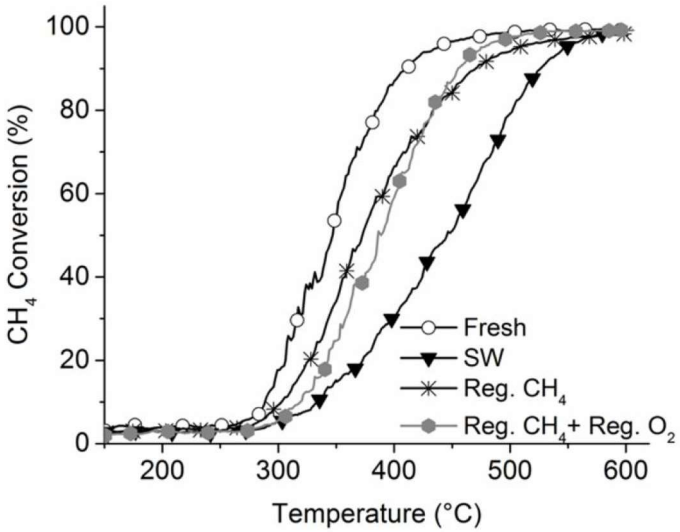

Figure 12. *CH_4 conversion as a function of temperature for the fresh, SW-treated and after that regenerated catalysts.*

For the CH_4 decomposition reaction over the 16-SO_3 encapsulated $Pd_{30}O_{44}/Al_2O_3$ catalyst, the structures of IS, TS and FS, together with the energy diagram of reaction pathway of the CH_4 oxidation on O*-O* site pairs of the $(SO_3)_{16}@Pd_{30}O_{44}/Al_2O_3$ catalyst are given in Figure 13. The initial optimized C-Pd distance is 3.65 Å with E^2_{ads}= 0.35 eV. Note that the cluster surface is not completely blocked by SO_3 enabling CH_4 adsorption. At TS, the C-H bond has elongated up to 2.01 Å before it binds with an O atom (labeled with O_3) of SO_3. The bond distances of H-O_3, H-O_1 C-O_2 (See labels in Figure 13b) are 0.99, 3.13 and 2.46 Å, respectively. The activation barrier is found to be 2.01 eV, much higher than that of the fresh $Pd_{30}O_{44}/Al_2O_3$ catalyst, which indicates chemical inactivity and agrees very well with the experimental results. This is expected based on the geometric (encapsulation) and electronic (charge transfer) properties of the $(SO_3)_{16}@Pd_{30}O_{44}/Al_2O_3$ catalyst system.

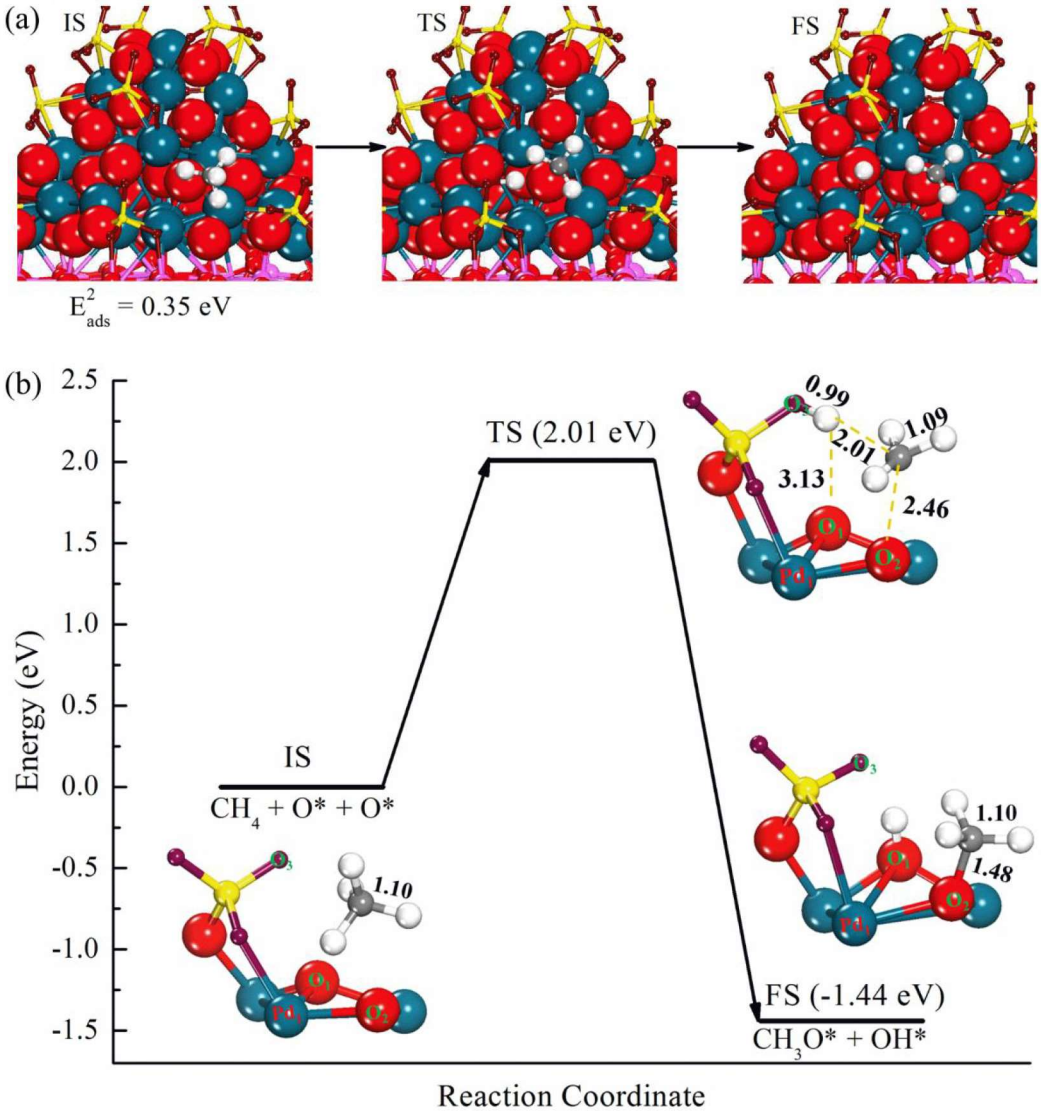

Figure 13. *CH_4 oxidation (CH_4 + O* + O* → CH_3O* + OH*) on $(SO_3)_{16}@Pd_{30}O_{44}/Al_2O_3(100)$: (a) Structures of the initial state (IS), transition state (TS), intermediate state (IM), and final state (FS). (b) Energy diagram of the reaction pathway on O*-O* site pairs (labeled with O_1-O_2). Color code: S, yellow; H, white C, gray; O (cluster), red; O (incoming), magenta; and Pd, dark green.*

CH_4 conversion is partially restored by the regeneration treatment under CH_4 conditions (Table 2 and Fig. 12). No full recovery was achieved, probably due to the small amount of remaining bulk $Al_2(SO_4)_3$, the formation of sulfur species on the palladium particles, and the partial reduction of PdO particles to Pd during the regeneration treatment. To reoxidize Pd to PdO, the catalyst was further regenerated under O_2 conditions and the catalyst further regenerated at 500 °C was selected for the performance tests to make sure of total reoxidation of Pd and at the same time to avoid possible sintering of the Pd/PdO particles at higher temperatures. According to our earlier studies [42], changes in the noble metal particles start at 700 °C in air. After the further regeneration in O_2 conditions, CH_4 conversion was at the same level with the regenerated (in CH_4 conditions) catalyst (Table 2 and Fig. 11). Thus, a small amount of bulk $Al_2(SO_4)_3$ seems to have a stronger effect on the catalyst performance than the state of palladium (Pd/PdO).

4 CONCLUSIONS

Sulfur deactivation and regeneration behavior of the Pd/Al_2O_3 natural gas oxidation catalyst was studied. The fresh and treated catalysts were characterized by TEM, XRD, FT-IR, and performance tests. The experimental characterizations were complemented by performing DFT-based simulations of PdO catalyst model structures with and without interacting SO_x species. During the sulfur treatment, PdO crystallites grew slightly. In addition, the formation of a small amount of bulk $Al_2(SO_4)_3$ was observed. Based on the DFT calculations, SO_x species showed a strong interaction with the catalyst. The saturation adsorption of $(SO_3)_n$ on $Pd_{30}O_{44}/Al_2O_3$ was reached at n=16, corresponding to the case where $Pd_{30}O_{44}$ is mostly encapsulated by SO_x. The catalyst structure retains, however, the original internal Pd-O geometry. During the regeneration treatment in CH_4 conditions, a part of bulk $Al_2(SO_4)_3$ was removed from the catalyst and PdO particles are partly reduced to metallic Pd. In addition to $Al_2(SO_4)_3$, sulfur species on the Pd particles were observed due to the migration of sulfate species from the support on the Pd particles during regeneration. To reoxidize Pd, the catalyst was further regenerated under O_2 conditions at various temperatures. After further regeneration, the catalyst had still a small amount of bulk $Al_2(SO_4)_3$ but sulfur species on the palladium particles disappeared.

The performance of the catalysts for CH_4 oxidation was studied theoretically and experimentally. Sulfur treatment and encapsulation of PdO cluster by SO_3 decreased the catalyst activity to convert CH_4. The conversion could be partly restored by the regeneration treatment in CH_4 conditions. Due to remaining bulk $Al_2(SO_4)_3$, the formation of sulfur species on the Pd particles, and the partial reduction of PdO particles to Pd during the regeneration treatment, no full recovery was achieved. After the further regeneration treatment under O_2 conditions (to reoxidize Pd to PdO), the CH_4 conversation was at the same level with the regenerated (in CH_4 conditions) catalyst. Thus, bulk $Al_2(SO_4)_3$ and sulfur species on the Pd particles seem to have a stronger effect on the catalyst performance than the state of palladium (Pd/PdO).

Acknowledgements

The Strategic funding tool of TUT Foundation is thanked for funding. The DFT calculations were performed at CSC - IT Center for Science, Espoo, Finland. We acknowledge the provision of facilities and technical support by Aalto University at OtaNano - Nanomicroscopy Center (Aalto-NMC).

References:

[1] R. van Basshuysen (Ed.), Natural Gas and Renewable Methane for Powertrains, Springer International Publishing, Switzerland, 2016, p. 482. doi:10.1007/978-3-319-23225-6.

[2] R.J. Farrauto, J.K. Lampert, M.C. Hobson, E.M. Waterman, Thermal decomposition and reformation of PdO catalysts; support effects, Appl. Catal. B Environ. 6 (1995) 263–270. doi:10.1016/0926-3373(95)00015-1.

[3] P. Gélin, M. Primet, Complete oxidation of methane at low temperature over noble metal based catalysts: a review, Appl. Catal. B Environ. 39 (2002) 1–37. doi:10.1016/S0926-3373(02)00076-0.

[4] S.K. Matam, M.H. Aguirre, A. Weidenkaff, D. Ferri, Revisiting the problem of active sites for methane combustion on Pd/Al_2O_3 by operando XANES in a lab-scale fixed-bed reactor, J. Phys. Chem. C. 114 (2010) 9439–9443. doi:10.1021/jp1019697.

[5] C.H. Bartholomew, Mechanisms of catalyst deactivation, Appl. Catal. A Gen. 212 (2001) 17–60. doi:10.1016/S0926-860X(00)00843-7.

[6] A.K. Datye, J. Bravo, T.R. Nelson, P. Atanasova, M. Lyubovsky, L. Pfefferle, Catalyst microstructure and methane oxidation reactivity during the Pd↔PdO transformation on alumina supports, Appl. Catal. A Gen. 198 (2000) 179–196. doi:10.1016/S0926-860X(99)00512-8.

[7] M. Lyubovsky, L. Pfefferle, Complete methane oxidation over Pd catalyst supported on α-alumina. Influence of temperature and oxygen pressure on the catalyst activity, Catal. Today. 47 (1999) 29–44. doi:10.1016/S0920-5861(98)00281-8.

[8] A. Baylet, P. Marecot, D. Duprez, P. Castellazzi, G. Groppi, P. Forzatti, In situ Raman and in situXRD analysis of PdO reduction and Pd^0 oxidation supported on γ-Al_2O_3 catalyst under different atmospheres, Phys. Chem. Chem. Phys. 13 (2011) 4607–4613. doi:10.1039/C0CP01331E.

[9] A.K. Neyestanaki, F. Klingstedt, T. Salmi, D.Y. Murzin, Deactivation of postcombustion catalysts, a review, Fuel. 83 (2004) 395–408. doi:10.1016/j.fuel.2003.09.002.

[10] J. Lampert, M. Kazi, R. Farrauto, Palladium catalyst performance for methane emissions abatement from lean burn natural gas vehicles, Appl. Catal. B Environ. 14 (1997) 211–223. doi:10.1016/S0926-3373(97)00024-6.

[11] A.T. Gremminger, H.W. Pereira de Carvalho, R. Popescu, J.-D. Grunwaldt, O. Deutschmann, Influence of gas composition on activity and durability of bimetallic $Pd\text{-}Pt/Al_2O_3$ catalysts for total oxidation of methane, Catal. Today. 258 (2015) 470–480. doi:10.1016/j.cattod.2015.01.034.

[12] D.L. Mowery, R.L. McCormick, Deactivation of alumina supported and unsupported PdO methane oxidation catalyst: the effect of water on sulfate poisoning, Appl. Catal. B Environ. 34 (2001) 287–297. doi:10.1016/S0926-3373(01)00222-3.

[13] O. Kröcher, M. Widmer, M. Elsener, D. Rothe, Adsorption and Desorption of SOx on Diesel Oxidation Catalysts, Ind. Eng. Chem. Res. 48 (2009) 9847–9857. doi:10.1021/ie900882p.

[14] N.M. Kinnunen, J.T. Hirvi, K. Kallinen, T. Maunula, M. Keenan, M. Suvanto, Case study of a modern lean-burn methane combustion catalyst for automotive applications: What are the deactivation and regeneration mechanisms?, Appl. Catal. B Environ. 207 (2017) 114–119. doi:10.1016/j.apcatb.2017.02.018.

[15] N. Luckas, F. Viñes, M. Happel, A. Desikusumastuti, J. Libuda, A. Görling, Density Functional Calculations and IR Reflection Absorption spectroscopy on the interaction of SO_2 with oxide-supported Pd nanoparticles, J. Phys. Chem. C. 114 (2010) 13813–13824. doi:10.1021/jp105097z.

[16] N. Luckas, K. Gotterbarm, R. Streber, M.P.A. Lorenz, O. Hofert, F. Vines, C. Papp, A. Gorling, H.-P. Steinruck, Adsorption and reaction of SO_2 on clean and oxygen precovered Pd(100)-a combined HR-XPS and DF study, Phys. Chem. Chem. Phys. 13 (2011) 16227–16235. doi:10.1039/C1CP21694E.

[17] K. Gotterbarm, N. Luckas, O. Höfert, M.P.A. Lorenz, R. Streber, C. Papp, F. Viñes, H.-P. Steinrück, A. Görling, Kinetics of the sulfur oxidation on palladium: A combined in situ x-ray photoelectron spectroscopy and density-functional study, J. Chem. Phys. 136 (2012) 94702. doi:10.1063/1.3687676.

[18] H.N. Sharma, V. Sharma, T. Hamzehlouyan, W. Epling, A.B. Mhadeshwar, R. Ramprasad, SOx Oxidation kinetics on Pt(111) and Pd(111): first-principles computations meet microkinetic modeling, J. Phys. Chem. C. 118 (2014) 6934–6940. doi:10.1021/jp501538v.
[19] F. Arosio, S. Colussi, G. Groppi, A. Trovarelli, Regeneration of S-poisoned Pd/Al_2O_3 and Pd/CeO2/Al2O3 catalysts for the combustion of methane, Top. Catal. 42 (2007) 405–408. doi:10.1007/s11244-007-0214-y.
[20] http://www.cp2k.org, (3.11.2017).
[21] J. VandeVondele, M. Krack, F. Mohamed, M. Parrinello, T. Chassaing, J. Hutter, Quickstep: Fast and accurate density functional calculations using a mixed Gaussian and plane waves approach, Comput. Phys. Commun. 167 (2005) 103–128. doi:10.1016/j.cpc.2004.12.014.
[22] J.P. Perdew, K. Burke, M. Ernzerhof, Generalized Gradient Approximation Made Simple, Phys. Rev. Lett. 77 (1996) 3865–3868. doi:10.1103/PhysRevLett.77.3865.
[23] S. Goedecker, M. Teter, J. Hutter, Separable dual-space Gaussian pseudopotentials, Phys. Rev. B. 54 (1996) 1703–1710. doi: 10.1103/PhysRevB.54.1703.
[24] J. VandeVondele, J. Hutter, Gaussian basis sets for accurate calculations on molecular systems in gas and condensed phases, J. Chem. Phys. 127 (2007) 114105. doi:10.1063/1.2770708.
[25] B.G. Lippert, J. Hutter and M. Parrinello, A hybrid Gaussian and plane wave density functional scheme, Mol. Phys. 92 (1997) 477–488. doi:10.1080/002689797170220.
[26] S. Grimme, Semiempirical GGA-type density functional constructed with a long-range dispersion correction, J. Comput. Chem. 27 (2006) 1787–1799. doi:10.1002/jcc.20495.
[27] W. Tang and E. Seanville and G. Henkelman, A grid-based Bader analysis algorithm without lattice bias, J. Phys. Condens. Matter. 21 (2009) 84204. http://stacks.iop.org/0953-8984/21/i=8/a=084204.
[28] R.F.W. Bader, A quantum theory of molecular structure and its applications, Chem. Rev. 91 (1991) 893–928. doi:10.1021/cr00005a013.
[29] G. Henkelman, B.P. Uberuaga, H. Jónsson, A climbing image nudged elastic band method for finding saddle points and minimum energy paths, J. Chem. Phys. 113 (2000) 9901–9904. doi:10.1063/1.1329672.
[30] M. Digne, P. Sautet, P. Raybaud, P. Euzen, H. Toulhoat, Use of DFT to achieve a rational understanding of acid–basic properties of γ-alumina surfaces, J. Catal. 226 (2004) 54–68. doi:10.1016/j.jcat.2004.04.020.
[31] A.F. Lee, K. Wilson, R.M. Lambert, C.P. Hubbard, R.G. Hurley, R.W. McCabe, H.S. Gandhi, The Origin of SO2 Promotion of Propane Oxidation over Pt/Al_2O_3 Catalysts, J. Catal. 184 (1999) 491–498. doi:10.1006/jcat.1999.2454.
[32] M. Honkanen, M. Kärkkäinen, T. Kolli, O. Heikkinen, V. Viitanen, L. Zeng, H. Jiang, K. Kallinen, M. Huuhtanen, R.L. Keiski, J. Lahtinen, E. Olsson, M. Vippola, Accelerated deactivation studies of the natural-gas oxidation catalyst—Verifying the role of sulfur and elevated temperature in catalyst aging, Appl. Catal. B Environ. 182 (2016) 439–448. doi:10.1016/j.apcatb.2015.09.054.
[33] H. Abdulhamid, E. Fridell, J. Dawody, M. Skoglundh, In situ FTIR study of SO_2 interaction with $Pt/BaCO_3/Al_2O_3$ NO_x storage catalysts under lean and rich conditions, J. Catal. 241 (2006) 200–210. doi:10.1016/j.jcat.2006.04.034.
[34] H. Mahzoul, L. Limousy, J.. Brilhac, P. Gilot, Experimental study of SO_2 adsorption on barium-based NOx adsorbers, J. Anal. Appl. Pyrolysis. 56 (2000) 179–193. doi:10.1016/S0165-2370(00)00090-5.
[35] S. Colussi, F. Arosio, T. Montanari, G. Busca, G. Groppi, A. Trovarelli, Study of sulfur poisoning on Pd/Al_2O_3 and $Pd/CeO_2/Al_2O_3$ methane combustion catalysts, Catal. Today. 155 (2010) 59–65. doi:10.1016/j.cattod.2009.02.019.
[36] T.-C. Yu, H. Shaw, The effect of sulfur poisoning on methane oxidation over palladium supported on γ-alumina catalysts, Appl. Catal. B Environ. 18 (1998) 105–114. doi:10.1016/S0926-3373(98)00031-9.
[37] M. Konsolakis, I.V. Yentekakis, G. Pekridis, N. Kaklidis, A.C. Psarras, G.E. Marnellos, Insights into the role of SO_2 and H_2O on the surface characteristics and de-N_2O efficiency of Pd/Al_2O_3 catalysts during N_2O decomposition in the presence of CH_4 and O_2 excess, Appl. Catal. B Environ.

138 (2013) 191–198. doi:10.1016/j.apcatb.2013.02.038.
[38] P. Gélin, L. Urfels, M. Primet, E. Tena, Complete oxidation of methane at low temperature over Pt and Pd catalysts for the abatement of lean-burn natural gas fuelled vehicles emissions: influence of water and sulphur containing compounds, Catal. Today. 83 (2003) 45–57. doi:10.1016/S0920-5861(03)00215-3.
[39] C. J. Zhang, P. Hu, The possibility of single C–H bond activation in CH_4 on a MoO_3-supported Pt catalyst: A density functional theory study, J Chem. Phys. 116 (2002) 4281. doi: 10.1063/1.1449942.
[40] A.A. Latimer, A.R. Kulkarni, H. Aljama, J.H. Montoya, J.S. Yoo, C. Tsai, F. Abild-Pedersen, F. Studt, J.K. Norskov, Understanding trends in C-H bond activation in heterogeneous catalysis, Nat Mater. 16 (2017) 225–229. http://dx.doi.org/10.1038/nmat4760.
[41] Y.-H. Chin, C. Buda, M. Neurock, E. Iglesia, Consequences of metal–oxide interconversion for C–H bond activation during CH_4 reactions on Pd catalysts, J. Am. Chem. Soc. 135 (2013) 15425–15442. doi:10.1021/ja405004m.
[42] M. Honkanen, T.W. Hansen, H. Jiang, M. Kärkkäinen, M. Huuhtanen, O. Heikkinen, K. Kallinen, J. Lahtinen, R.L. Keiski, J.B. Wagner, M. Vippola, Electron microscopic studies of natural gas oxidation catalyst – Effects of thermally accelerated aging on catalyst microstructure, J. Catal. 349 (2017) 19–29. doi:10.1016/j.jcat.2017.03.003.